Valley Hall effect and kink states in topolectrical circuits

S. M. Rafi-Ul-Islam,[1,*] Zhuo Bin Siu,[1,†] Haydar Sahin,[1,2,‡] and Mansoor B. A. Jalil[1,§]
[1]*Department of Electrical and Computer Engineering, National University of Singapore, Singapore 117583, Republic of Singapore*
[2]*Institute of High Performance Computing, A*STAR, Singapore 138632, Republic of Singapore*

(Received 18 June 2022; accepted 26 January 2023; published 13 February 2023)

We investigate the emergence of topological valley Hall and kink states in a two-dimensional topolectrical (TE) model as a result of broken chiral and reflection symmetries. The TE system consists of two segments hosting distinct topological states with opposite (similar) signs of the valley Hall index, and separated by a heterojunction to exhibit valley kink (Chern insulating) phases at the interface. In the practical circuit, the valley Hall index can be flipped between the two segments by modulating the on-site potential on the sublattice nodes of the respective segments. The presence of grounding connections in the circuit array subsequently leads to the emergence of gapped and gapless valley and kink states in the admittance spectra. These topological modes can be detected electrically by the impedance readouts of the system, which can be correlated to its admittance spectra. Finally, we confirm the robustness of the valley Hall and kink states via realistic LTspice simulation, taking into account the tolerance windows and parasitic effects inherent in circuit components. Our study demonstrates the applicability of TE circuit networks as a platform to realize and tune valley-dependent and kink topological phenomena.

DOI: 10.1103/PhysRevResearch.5.013107

I. INTRODUCTION

The study of topological phases has emerged as a key topic in condensed-matter physics due to the unconventional properties of such phases [1–3], which possess a nontrivial band topology. The valley property meanwhile constitutes a new degree of freedom that can be found in lattice models with various symmetries [4–7]. This additional valley degree of freedom is useful in various technologically significant applications such as robust electronic transport [8,9], energy propagation [10], and information processing [11,12]. As a result, the valley degree of freedom has given rise to a new branch of technology named "valleytronics" [13–15] that has found applications in many existing fields such as photonics [16,17], metamaterials [18,19], condensed matter [20], acoustics [21,22], and next-generation quantum computing [23–26]. Breaking the inversion symmetry in a lattice model results in a valley-dependent Hall conductivity and a quantum valley Hall effect [27,28]. The inversion symmetry can be broken by inducing alternating mass terms in the lattice Hamiltonian [29]. A domain wall-type interface is created when two lattice segments with opposite valley responses are joined together. Robust valley kink states appear at the interfaces of such heterojunctions [30,31]. These novel valley kink states are useful in many promising phenomena such as Klein tunneling [32–36], anti-Klein tunneling [37], spin-valley locking [38,39], and quantum memory [40,41].

More recently, topological boundary states have been realized in many Hermitian [42,43] and non-Hermitian systems [44–47]. These topologically nontrivial boundary states are characterized by the topological index (i.e., Chern number [48] and Hall conductivity [49]) of their gapped bulk energy bands, and they exhibit gapped and gapless states on their boundaries depending on the model parameters. These novel topological boundary phases and valley Hall states have recently been demonstrated in different platforms such as photonic systems [24,50,51], metamaterials [19,22,52,53], and quantum wells [54]. Although boundary states and valley kink modes promise to bring dramatic changes to existing technologies, it is difficult to realize and observe multiple topological valley and boundary phases in the same lattice model because of difficulties in the dynamical modulation of the system parameters (e.g., fixed lattice constants and weak spin-orbit coupling). Additionally, all these platforms involve experimentally complex sample preparation, which is very vulnerable to perturbations and impurities.

Lattice arrays comprising electrical components such as inductors and capacitors known as topolectrical (TE) circuits [37,55–59] have become the frontier experimental testbed in the quest for alternative platforms to study different topological states. Compared to other platforms, TE circuits offer better tunability of system parameters such as the interaction strength and phases. Recently, many exotic and novel features such as edge states [56,60,61], corner states [62,63], quantum spin Hall states [64,65], chiral magnetic effects [66,67],

*e0021595@u.nus.edu
†elesiuz@nus.edu.sg
‡sahinhaydar@u.nus.edu
§elembaj@nus.edu.sg

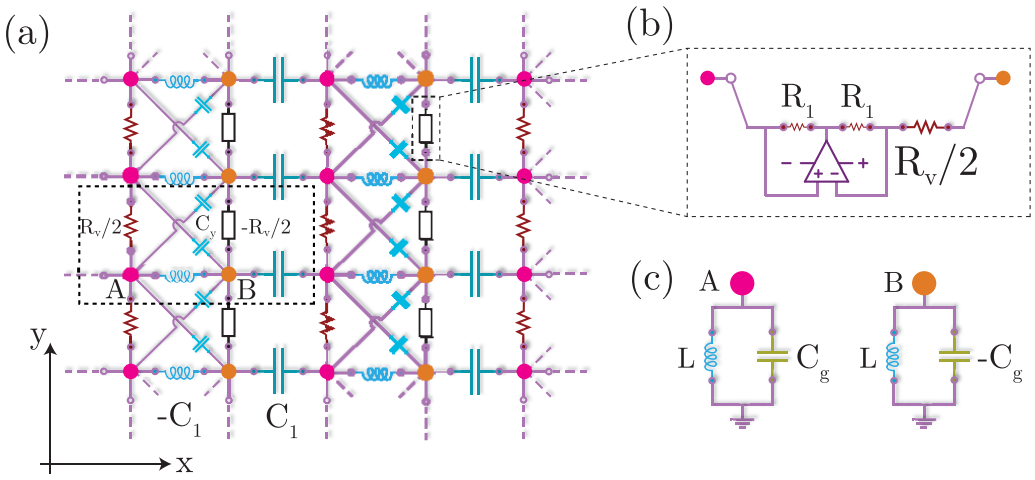

FIG. 1. (a) Schematic of the valley TE lattice model that hosts valley-dependent topological phases. Here, the magenta and orange circles represent the A and B sublattice nodes, respectively. The unit cell is delineated by the dotted box. The two alternating sublattices are connected by a capacitor C_1 and inductor of $-C_1$ [i.e., an inductance of $1/(\omega^2 C_1)$] along the x direction for the intracell and intercell connections, respectively. Along the y direction, neighboring nodes on opposite sublattices are connected by a capacitor C_y and nodes on the same sublattice connected through alternating sequences of resistive elements $\pm R_v/2$. (Note that there is a π phase difference in the resistive coupling between the A-A and B-B connections along the y direction within the same unit cell.) (b) We can make use of the negative resistance converter to realize the π phase difference between the A-A and B-B connections along the y direction. The combination of resistors R_1 and $R_v/2$ along with an ideal operational amplifier with supply voltages $V-$ and $V+$ acts as a negative resistance converter with current inversion. (c) Grounding mechanism of our valley TE circuit. All nodes are connected to ground by a common capacitor (C) and inductor (L). Furthermore, each A and B node is coupled to the ground with the same magnitude but opposite signs of the coupling strength by an on-site capacitor and an inductor, respectively.

topological photonic states [68], and nodal ring states [69–72] have been proposed in electrical circuit networks [36,56,58,59,73]. The topological states depend on the connectivity between the electrical components rather than their relative locations in real space. The TE circuit models also provide better flexibility in varying the system parameters coupled with the convenient and accurate readout of system characteristics.

In this paper, we design and propose a general framework to realize various topological valley phases, kink states, and Chern insulating phases based on the electrical responses in a two-dimensional TE circuit model. We have explained in detail the fundamental relationship between the admittance band structure and the impedance profiles through the circuit Green's function in our previous works [36,55,57]. By tuning the on-site interaction strength on the different sublattice nodes, we obtain a transition from gapless to gapped edge states in the admittance spectra. The valley-dependent Hall conductivity is calculated using the analogous Kubo formula and verified through the impedance spectrum. We study the valley kink (Chern insulating) states that result from cascading two TE segments with opposite (same) signs of the valley Hall responses together. The opposite signs of the valley Hall responses can be realized by reversing the sign of the on-site capacitance, and hence the Laplacian mass term, on both sides of the heterojunction. Both gapless and gapped kink states can be obtained by varying the relative strengths of the on-site capacitance to the resistive coupling strength. The topological kink states are localized at the interface of the heterojunction and can be distinguished by their terminal impedances. Since such TE circuit models can be implemented in typical breadboards or printed circuit boards with basic electrical components, our model not only opens new experimental possibilities and directions for the realization of various topological valley phases, but also helps in the design of multifunctional valleytronic devices.

II. TOPOLECTRICAL VALLEY CIRCUIT MODEL

Consider the TE circuit model consisting of basic electrical components such as inductors and capacitors in Fig. 1. An AC current of angular frequency ω flows through the circuit, which comprises two different types of sublattice nodes labeled as the A- and B-type nodes, respectively, indicated as the magenta and orange circles in the figure. Along the x direction, the two adjacent sublattice nodes within the same unit cell are connected by an inductor with an admittance equivalent to that of a capacitance of $-C_1$ [i.e., an inductance of $1/(\omega^2 C_1)$]. The adjacent nodes in neighboring unit cells are connected by a capacitance C_1 [see Fig. 1(a)]. Along the y direction, adjacent nodes on different sublattices are connected by a capacitance C_y while nodes on the same sublattice are connected through alternating sequences of positive and negative resistive elements $R_v = \frac{1}{i\omega r}$, where r is a resistance. Note that the A-A and B-B couplings along the y direction have a relative π phase difference in their resistive couplings within the same unit cell. Such π phases in the resistive elements can be obtained using negative resistance converters (NRCs) [see Fig. 1(b)], which break the reflection symmetry along the y direction. Each A and B node is connected to the ground via a common capacitor C and inductor L. Each A and B node is further grounded by another on-site potential capacitor C_g and inductor equivalent to a capacitance of $-C_g$, respectively. The common grounding inductor (L) is used to adjust the offset

of the admittance dispersion to a common value for all nodes [36,44,74].

III. LAPLACIAN PHASES

The TE circuit can be described by its Laplacian, which is analogous to the tight-binding Hamiltonian in quantum physics [36,55,56]. The Laplacian at the resonant frequency of $\omega_r = 1/\sqrt{2C_yL}$ multiplied by $i\omega_r$, which we shall refer to from now on as the normalized Laplacian for short, is given by

$$L_{\rm TE}(k_x, k_y) = [-C_1 + C_1\cos(k_x) + 2C_y\cos(k_y)]\sigma_x + C_1\sin(k_x)\sigma_y + [C_g + R_v\sin(k_y)]\sigma_z, \quad (1)$$

where $\sigma = (\sigma_x, \sigma_y, \sigma_z)$ are the Pauli matrices denoting the A/B sublattice degree of freedom.

The circuit hosts both topologically trivial and nontrivial phases depending on the relative magnitudes of the circuit parameters C_g, R_v, C_1, and C_y. We first investigate the transition points between the topologically trivial and nontrivial phases in the (C_g, R_v, C_1, C_y) parameter space at which the eigenvalue spectrum of the Laplacian in Eq. (1) becomes gapless. This happens when the coefficients of all the Pauli matrices in Eq. (1) are simultaneously zero for some real $\vec{k}$ in the Brillouin zone. For the coefficient of σ_z to be zero, we require $k_y = \pm\sin^{-1}(C_g/R_v)$, which has a real solution when $|R_v| \geqslant |C_g|$, while the coefficient of σ_y is zero when $k_x = 0, \pi$. Substituting $k_x = \pi$ and $k_y = \cos^{-1}(C_g/R_v)$ into the coefficient of σ_x in Eq. (1), we have $C_1[1-\cos(k_x)] + 2C_y\cos(k_y) = 2[-C_1 \pm C_y\sqrt{1-(C_g/R_v)^2}]$. This is zero when $(C_1/C_y)^2 + (C_g/R_v)^2 = 1$. Thus, the phase transition points occur at $(C_1/C_y)^2 + (C_g/R_v)^2 = 1$ and at $|C_g| = |R_v|$.

Figure 2(a) shows the surfaces on which these phase transition points lie in the (C_g, R_v, C_1) space at $C_y = 1.5$ μF. To determine which side of the phase transition surfaces corresponds to the topologically nontrivial phases, we numerically calculated the Chern numbers of the normalized Laplacian using the Fukui-Hatsugai-Suzuki algorithm [75], which provides a numerical means of evaluating the Chern number on a discretized lattice. Figure 2(b) shows the Chern numbers at $C_y = 0.5$ μF and $C_g = 0.1$ μF. The topologically nontrivial phases with finite Chern numbers occur at the intersections of $(C_1/C_y)^2 < 1 - (C_g/R_v)^2$ and $|R_v| > |C_g|$.

The latter condition can also be obtained analytically by considering the linear response of the system. Expanding Eq. (1) around $\vec{k}_0 = (0, \eta\frac{\pi}{2})$, $\eta = \pm 1$, we obtain

$$L^{\eta}_{\rm DP}(\vec{q}) = 2\eta C_y q_y\sigma_x + C_1 q_x\sigma_y + (C_g + \eta R_v)\sigma_z, \quad (2)$$

where $\vec{q} \equiv \vec{k} - \vec{k}_0$. One may thus identify the two $\vec{k}_0$ points as the Dirac points (DPs) of massive Dirac fermion Hamiltonians Eq. (2) associated with the two valleys, so that η takes the meaning of a valley index, where $\eta = +1(-1)$ denotes the K and K' valley index, respectively. The low-admittance dispersion is given by

$$\epsilon^{\eta}_{\pm} = \pm\sqrt{(2C_yq_y)^2 + (C_1q_x)^2 + (C_g + \eta R_v)^2}, \quad (3)$$

where $\pm$ denotes the particle- and hole-like bands, respectively. In a condensed matter system, the Hall conductivity σ_{xy} at each valley can be calculated through the standard Kubo formula [76] as

$$\sigma^{\eta}_{xy} = \int \frac{dq^2}{\pi^2}\frac{1}{(\epsilon^{\eta}_{+} - \epsilon^{\eta}_{-})^2}{\rm Im}(M^{\eta+}_x(\vec{q})M^{\eta-}_y(\vec{q})), \quad (4)$$

where $M^{\eta\pm}_x(\vec{q}) = \langle +, \vec{q}, \eta|(\partial_{q_x}L^{\eta}_{\rm DP})|-, \vec{q}, \eta\rangle$ and $M^{\eta\mp}_y(\vec{q}) = \langle +, \vec{q}, \eta|(\partial_{q_y}L^{\eta}_{\rm DP})|-, \vec{q}, \eta\rangle$. Here, $|\pm, \vec{q}, \eta\rangle$ is the right eigenvector of Eq. (2), and $\langle\pm, \vec{q}, \eta|$ is its Hermitian conjugate. Even though the notion of a Hall conductivity is not applicable in a TE context, the direct analogy between the TE Laplacian matrix and the Hamiltonian in a condensed matter system implies that the presence of any topological edge states predicted from the Hall conductivity in the latter will directly translate into the presence of edge modes in the former when Eq. (4) is applied to the eigenvectors of the circuit Laplacian. Therefore, we shall borrow the terminology from condensed matter physics for the quantity calculated using Eq. (4) and continue to refer to it as the valley Hall conductivity with the understanding that it does not physically refer to a Hall current in the TE context.

For our Laplacian, the valley-dependent Hall conductivity can be evaluated as

$$\sigma^{\eta}_{xy} = -\frac{1}{8\pi^2}{\rm Sgn}C_1C_y(\eta C_g + R_v). \quad (5)$$

We define the valley Hall conductivity as $\sigma^{\rm valley}_{xy} \equiv \sigma^{\eta=1}_{xy} - \sigma^{\eta=-1}_{xy}$ and the Chern number as $\sigma^{\rm valley}_{xy} \equiv \sigma^{\eta=1}_{xy} + \sigma^{\eta=-1}_{xy}$. For $|C_g/R_v| < 1$, σ^{η}_{xy} has the same sign for both values of $\eta = \pm 1$. This results in a finite Chern number, which agrees with the numerical results of a finite Chern number in Fig. 2(a) for large $|C_1|$ and $|R_v|$ and corresponds to a Chern insulator state. [The Chern number is 0 there at small $|C_1|$ due to the contributions of the Berry curvature near $k_x = \pi$ and $k_y = \cos^{-1}(C_g/R_v)$, where the bands may touch if $(C_1/C_y)^2 + (C_g/R_v)^2 = 1$. These contributions were numerically found to be negligibly small at large C_1 and R_v.]

In contrast, when $|C_g/R_v| > 1$, the two valleys have opposite signs of Hall conductivities. Although the Chern number is zero in this case, there is a finite quantum valley Hall conductivity. We hence refer to this regime as the valley Hall regime. As we shall show shortly, edge states will still emerge when boundaries are introduced along certain directions, although these edge states do not cross the band gap. Figure 2(c) shows the dispersion relations at representative points on the R_v-C_1 plane for nanoribbon geometries of the TE circuit in which the circuits have infinite length along the x direction and 10 unit cells in the y direction (left), and in which the circuits have infinite length along the y direction and 10 unit cells in the x direction (right). (The admittance dispersion is the TE analog of the energy dispersion in quantum-mechanical systems.) In general, the dispersion relations for the finite-x and finite-y nanoribbons appear markedly different from one another, although their topological character remains unchanged when the finite direction is exchanged. Points (i) and (iii) in Fig. 2(b) exemplify the $|R_v| < |C_g|$ scenario, with $|C_1| > |C_y|$ at point (i) and $|C_1| < |C_y|$ at point (iii). At both of these points, no edge states exist when the nanoribbon confinement direction is along the y direction. However, edge states emerge when the nanoribbon confinement is along the x direction. The edge states are more

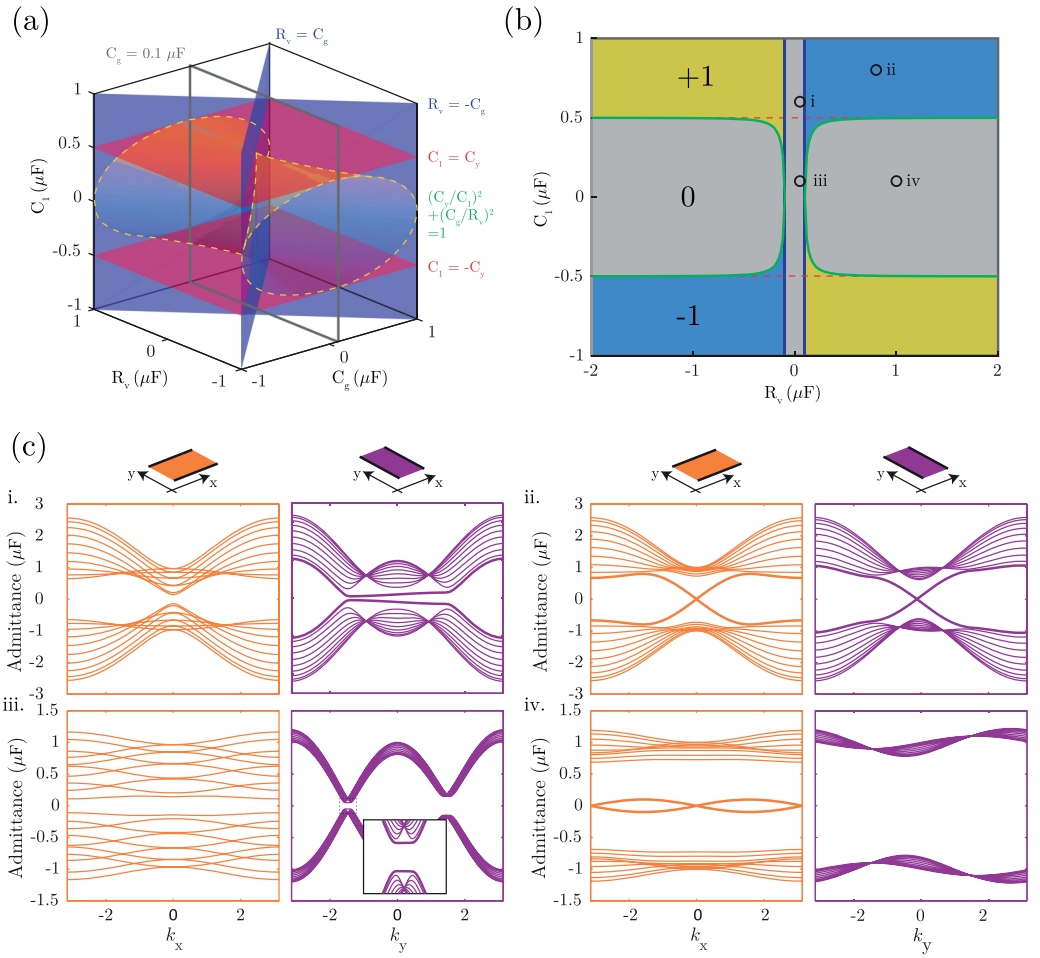

FIG. 2. (a) The phase transition surfaces in (C_g, R_v, C_1) space at a fixed $C_y = 0.5$ μF. The green surfaces outlined by the dotted lines denote the $(C_1/C_y)^2 + (C_g/R_v)^2 = 1$ surfaces, and the blue planes the $|R_v| = |C_g|$ planes. The unfilled orange box denotes the $C_g = 0.1$ μF plane shown in panel (b). (b) The Chern numbers as functions of C_1 and R_v at $C_g = 0.1$ μF and $C_y = 0.5$ μF. The gray areas denote the topologically trivial phase where the Chern number is zero. The dark blue lines denote the $|R_v| = |C_g|$ lines, and the green lines are the projections of $(C_1/C_y)^2 + (C_g/R_v)^2 = 1$ onto the $C_g = 0.1$ μF plane. The points (i)–(iv) denote the values of R_v and C_g at which the dispersion relations in the finite x-width and finite y-width nanoribbon geometries are plotted in panel (c). The (C_g, C_y, C_1, R_v) values of these points are (i) (0.1, 0.5, 0.6, 0.025) μF, (ii) (0.1, 0.5, 0.8, 0.3) μF, (iii) (0.1, 0.5, 0.1, 0.025) μF, and (iv) (0.1, 0.5, 0.1, 0.5) μF. (c) Admittance band dispersions of the TE model at the four (C_1, R_v) points denoted in panel (b) in the nanoribbon geometry with (left) infinite length along the x direction and 10 unit cells along the y direction, and (right) infinite length along the y direction and 10 unit cells along the x direction. The nanoribbon geometries are schematically illustrated by the schematics at the top of the figure where the thick black borders at the edges denote open boundary conditions at the edges while the borderless edges extend to infinity. The thick lines in the admittance plots denote the edge states. Note that those edge states associated with (i), (ii), and (iv) are trivial because they do not cross the band gap, while that of (iii) are nontrivial and band-gap crossing.

prominent at $|k_y| < \pi/2$ in the case of $|C_1| > |C_y|$ corresponding to point (i), whereas the edge states are confined to a narrow range of k_y in the vicinity of $|k_y| = \pm\pi/2$ in the case of $|C_1| < |C_y|$ corresponding to point (iii). Point (iv) corresponds to the scenario of $|R_v| > |C_g|$, $(C_y/C_1)^2 > 1 - (C_g/R_v)^2$. In contrast to points (i) and (iii) discussed previously, edge states appear on point (iv) only when the nanoribbon confinement direction is in the x direction, but not in the y direction. Note that the edge states corresponding to (i), (iii), and (iv) do not cross the band gap. Finally, point (ii) exemplifies the Chern insulator phase, which exists when $|R_v| > |C_g|$, $(C_y/C_1)^2 < 1 - (C_g/R_v)^2$. Edge states that cross the bulk gap are present for both nanoribbon confinement directions. In the remainder of this paper, we will focus on the phases exemplified by points (ii) (Chern insulator) and (i) (valley Hall insulator) for the case of $|C_1| > |C_y|$.

To further investigate the effect of C_g and R_v on the TE model when $|C_1| > |C_y|$, we simulated the circuit in LTspice with realistic device parameters and plot the admittance and impedance spectra as functions of the wave vector k_y for open boundary conditions along the x direction [see Figs. 3(a)–3(c)]. The impedance between any two lattice sites p and q in the TE network model is given by

$$\begin{aligned} Z_{pq} &= (L_{\mathrm{TE}})^{-1}_{pp} - (L_{\mathrm{TE}})^{-1}_{pq} + (L_{\mathrm{TE}})^{-1}_{qq} - (L_{\mathrm{TE}})^{-1}_{qp} \\ &= \sum_{k=1}^{N} \frac{|\phi_{kp} - \phi_{kq}|^2}{\epsilon_k}, \end{aligned} \tag{6}$$

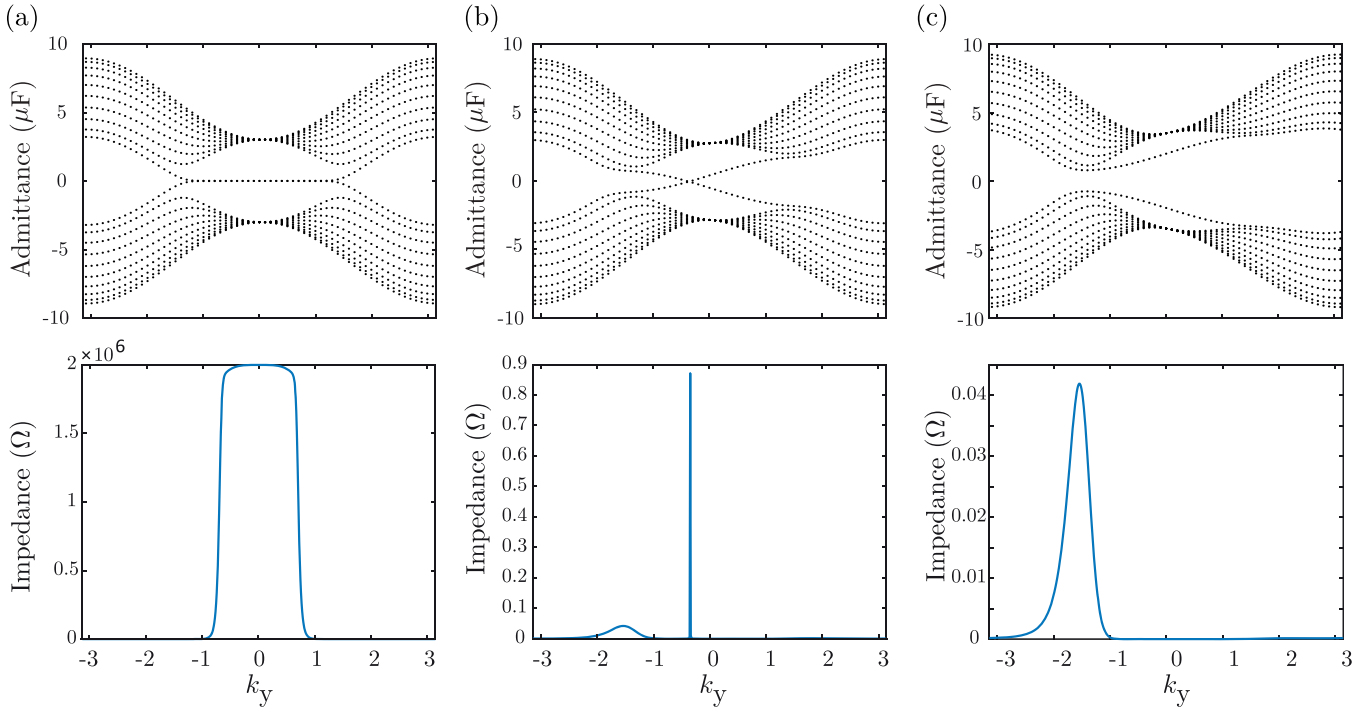

FIG. 3. Simulated admittance and impedance profiles of the valley TE circuit. The simulation is performed via the electric circuit simulation software LTspice. The top rows show the admittance dispersion relations of x-confined nanoribbons with 10 unit cells along the x direction at the resonant frequency $f = 25.250$ Hz. For a realistic simulation, the components are selected from the LTspice component database i.e., $C_1 = 3$ μF (2× Murata GRM033R60G155ME14D), and $C_y = 1.5$ μF (Murata GRM033R60G155ME14D) for (a) edge states with $C_g = 0$ μF and $R_v = 0$, (b) the Chern insulator phase $C_g = 0.56$ μF (KEMET C1206C564K3RACTU) and $R_v = 2$ μF, and (c) the Hall valley phase with $C_g = 2.2$ μF (KEMET C0603C225K9PAC) and $R_v = 0.5$ μF. For the common grounding inductors, $L = 10$ μH (Würth Elektronik 744042100) is used. To realize the negative resistive element R_v, we performed the simulation with the high precision operational amplifier LT1056. The bottom rows show the respective spectra of the impedances measured between the two edges of the nanoribbons.

where ϕ_{ij} is the value of the ith eigenvector at the jth lattice point, and ϵ_i is the ith nonsingular eigenenergy of the Laplacian matrix. Note that the LTspice simulations took into account tolerance windows and parasitic effects. Even after including such effects/imperfections, the topological behavior remains largely unaffected.

In the upper plot in Fig. 3(a), we find well-defined edge states for zero C_g and R_v. Moreover, the whole admittance spectrum is symmetric about the zero admittance line. This is due to the chiral symmetry of the Laplacian $\mathcal{C}L_{\mathrm{TE}}(\vec{k})\mathcal{C}^{-1} = -L_{\mathrm{TE}}(\vec{k})$, where $\mathcal{C} = \sigma_z$ is the chiral inversion operator. However, the boundary mode evolution differs for a finite mass term, i.e., $(C_g + \eta R_v)$ in Eq. (2). When $|C_g| < |R_v|$, gapless edge modes emerge [see Fig. 3(b)], where the zero-energy edge states split into two tilted boundary states that intersect each other. However, when the resistive coupling becomes stronger than the on-site capacitor (i.e., $|C_g| > |R_v|$), gapped boundary modes appear, as shown in Fig. 3(c). Interestingly, a finite mass term breaks the symmetry of the admittance dispersion about the $E = 0$ line [Figs. 3(b) and 3(c)].

The impedance spectra for Figs. 3(a)–3(c) are shown in the lower plots of the corresponding panels. The nearly zero-admittance edge states in Fig. 3(a) are marked by a very large impedance for $|k_y| \lesssim \pi/2$, which agrees with the inversely proportional relation between the eigenvalue (admittance) and the impedance in Eq. (6). However, the impedance falls significantly in the presence of a mass term in the circuit Laplacian, and only discrete impedance peaks are found when the admittance gap between the two bands reaches close to zero [see Figs. 3(b) and 3(c)]. The gapless and gapped edge states are indicated by comparatively large and small impedance peaks, respectively [compare the sharp peak in Fig. 3(b) with the broader lower peak of Fig. 3(c)]. The close correspondence between the admittance spectra and impedance readouts obtained from the LTspice simulation demonstrates the experimental realization of valley-dependent features and their electrical characterization under realistic conditions.

IV. CHERN AND VALLEY KINK STATES

In the previous section, we studied the relation between the valley-dependent topological phases and the emergence of edge states. In this section, we study the evolution of the boundary states in a heterojunction between two TE segments in which the Chern numbers or Hall conductivities of each valley have opposite signs in the two segments. More explicitly, we realize a topolectrical valley kink state at the domain-wall-like interface between two TE circuit arrays with opposite signs of the Chern numbers or Hall conductivities as shown in Fig. 4. Such heterojunctions can be realized by simply reversing the sign of the on-site capacitance C_g between the two array segments for a fixed $|R_v| < |C_g|$. The TE lattice on the left and right sides of the interface have

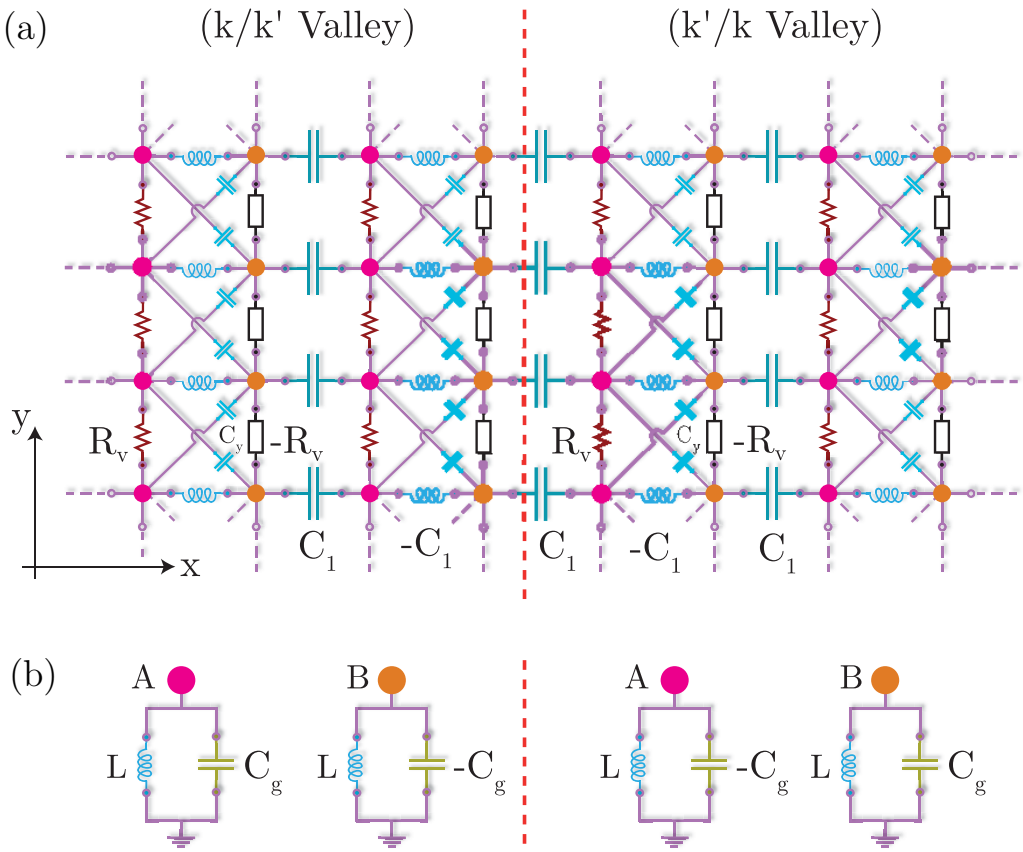

FIG. 4. Schematic of a TE circuit heterojunction that exhibits kink states. (a) Chern/valley kink circuit. (b) Schematic of the wiring between each node and the ground in the two regions. Note that the on-site potential parameter (i.e., C_g) changes sign between the two regions. This guarantees that the Hall conductivity of each of the valleys switches sign across the heterojunction interface. All the other parameters are the same in both regions.

the same model parameters except for the on-site potential C_g, which is positive and negative on the left and right sides, respectively. Such a sign change in one of the mass parameter terms (i.e., C_g) across the heterojunction will induce valley-dependent kink states localized at the interface. Here, we focus on heterojunctions where the interface is parallel to the y direction.

We first focus on the Chern kink states that are at the interface between two TE segments with finite Chern numbers of opposite signs. Figure 5 shows the admittance dispersions of the left [Fig. 5(a)] and right [Fig. 5(b)] halves of the heterojunction [Fig. 5(c)] in isolation from each other, and that of the entire heterojunction when both halves of the heterojunction are connected together. In the particular heterojunction under consideration, the TE circuit array to the left of the heterojunction has a positive C_g while the right half has a negative C_g of the same magnitude, and $C_1 > C_y$, which puts the system into the Chern insulator regime. One way of ascertaining the topological character of a particular state is to plot its spatial distribution. Hence, the square of the voltage amplitudes summed over the A and B nodes in each unit cell is plotted for some of the bands as a function of the x coordinate across the transverse width of the TE. The square of the voltage amplitude constitutes the TE analogs of the quantum-mechanical probability densities $\psi_x^\dagger \psi_x$ for states described by the wave-function spinor ψ_x, and they shall be loosely referred to as "probability densities" for brevity henceforth. The probability densities in panels (a) and (b) show that the bands crossing the admittance band gap (ii, iii, vi, and vii) consist of edge states exhibiting edge localization. Furthermore, when the edge states have positive (negative) k_y slopes, i.e., ii and vi (iii and vii), the corresponding states are localized on the left (right) edges of the nanoribbon. The other bands labeled as i, iv, v, and viii consist of bulk states where the highest probability densities occur near the center of the nanoribbon and away from the edges. Comparing Figs. 5(a) and 5(b), we find that the k_y dispersion of nanoribbons with opposite signs of C_g are reflections of each other about the k_y axis. This reflection symmetry can be understood from the form of the Laplacian Eq. (1): the Laplacian is invariant upon the simultaneous replacement of $C_g \to -C_g$ and a reflection about the x axis, which brings $k_x \to -k_x$ and $\sigma_{y,z} \to -\sigma_{y,z}$.

When the two halves of the heterojunction are connected together in the heterojunction, the resultant dispersion relation of the bulk bands is roughly given by the superposition of the bulk band dispersions in the isolated halves of the heterojunction, as shown in Fig. 5(c). There is a slight increase in the energy separation between corresponding pairs of bulk bands from each of the isolated halves in the heterojunction due to the band anticrossing. Note that the edge states localized away from the heterojunction interface in either half of the TE heterojunction circuit are not significantly perturbed when

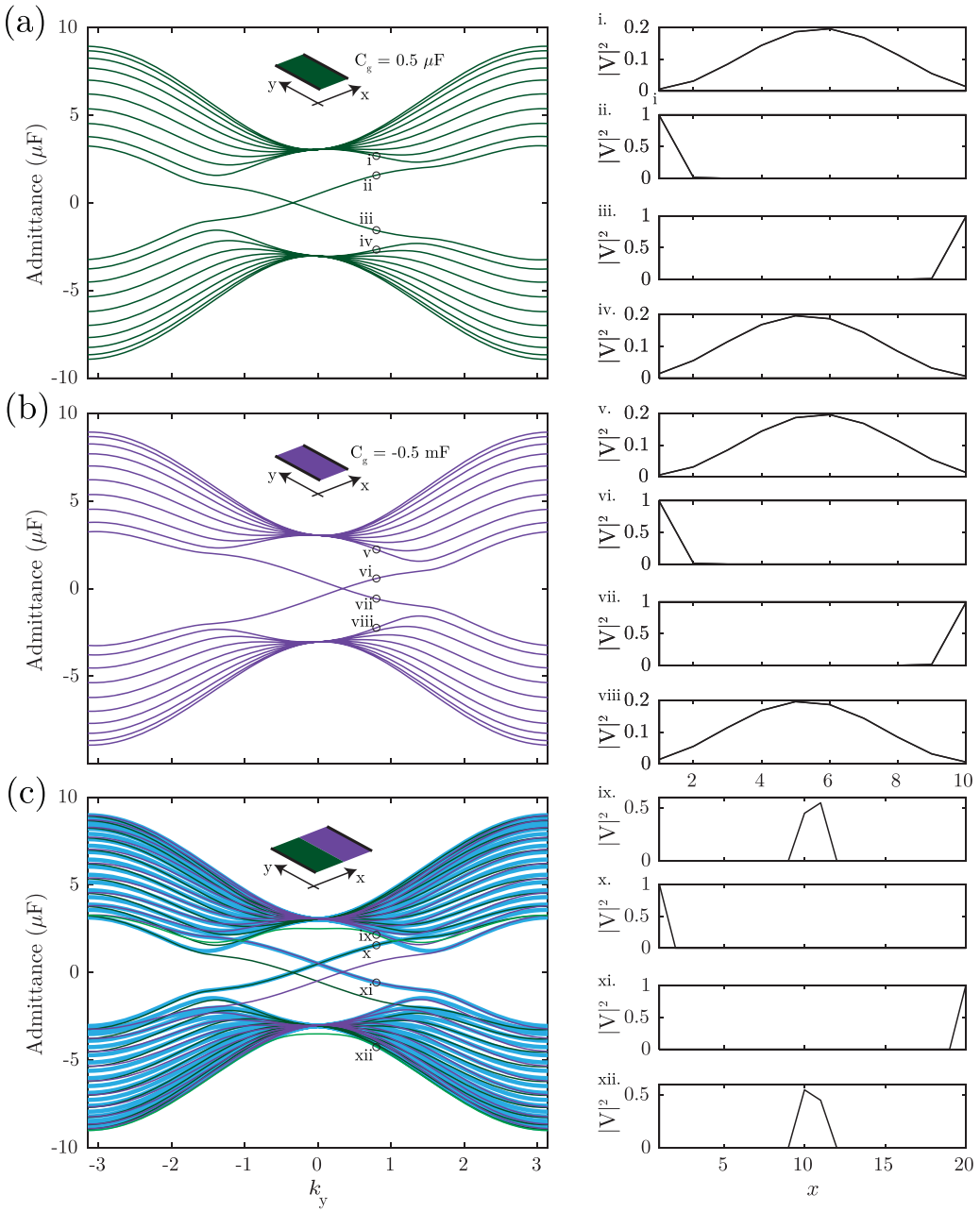

FIG. 5. The plots on the left show the admittance dispersions for TE circuits with $C_1 = 3$ μF, $R_v = 0.75$ μF, $C_y = 1.5$ μF for (a) a 10-unit-cell-wide $C_g = 0.5$ μF nanoribbon, and (b) a 10-unit-cell-wide $C_g = -0.5$ μF nanoribbon. The thicker lines in panel (c) show the dispersion relation of the heterojunction consisting of the nanoribbon in (a) on the left and the nanoribbon in (b) on the right connected together along the y direction with the dispersion relations of the isolated left and right nanoribbons superimposed as thinner lines. The thicker green lines denote the valley kink states. The plots on the right indicate the voltage amplitudes of the bands labeled i–xii in the dispersion relations at $k_y = 0.8$.

the heterojunction is formed. For instance, the dispersion and spatial distribution of band xi (x) is virtually identical to that of band vii (ii), which is localized at the right (left) edge of the isolated half circuits. In contrast, the edge states of the isolated halves localized at the edges adjacent to the heterojunction interface (iii and viii) have disappeared in the heterojunction. They are replaced by bands ix and xii that emerge in the TE heterojunction circuit, which do not have corresponding counterparts in the isolated halves of the heterojunction circuit. These new bands correspond to the valley kink states localized at the heterojunction interface as depicted in the spatial variation of $|V|^2$ in Fig. 5(c).

Analogous trends are observed in the valley Hall regime when two TE segments with zero Chern numbers but opposite signs of the valley Hall conductivities are connected together to form a heterojunction. Figure 6 shows the admittance dispersions of the left [Fig. 6(a)] and right [Fig. 6(b)] halves of an exemplary heterojunction in isolation from each other, and that of the entire heterojunction when both halves are connected together [Fig. 6(c)]. Each half of the heterojunction

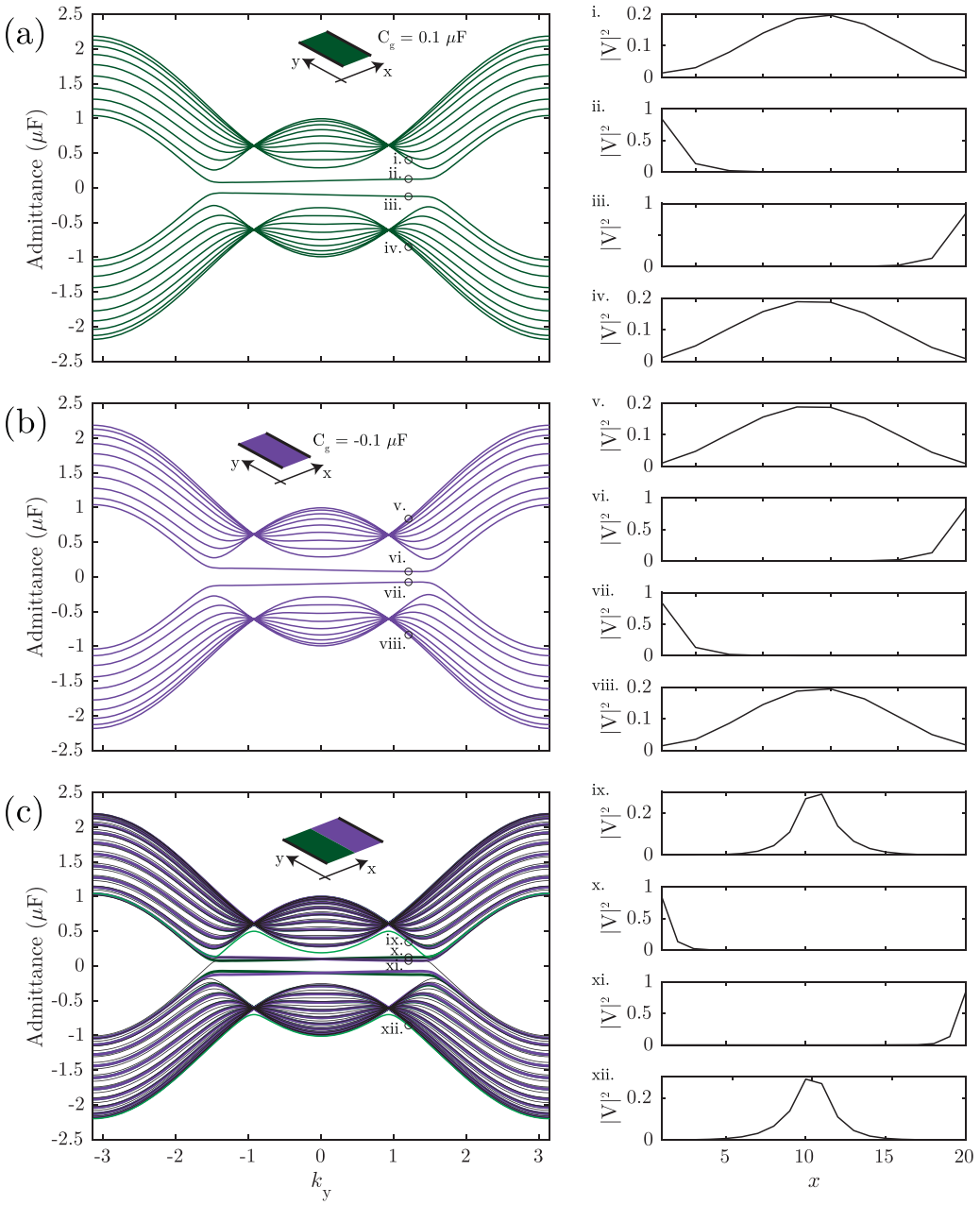

FIG. 6. The plots on the left show the admittance dispersions for TE circuits with $C_1 = 0.6$ μF, $R_v = 0.025$ μF, $C_y = 0.5$ μF for (a) a 10-unit-cell-wide $C_g = 0.1$ μF nanoribbon, and (b) a 10-unit-cell-wide $C_g = -0.1$ μF nanoribbon. The thicker lines in panel (c) show the dispersion relation of the heterojunction consisting of the nanoribbon in (a) on the left and the nanoribbon in (b) on the right connected together along the y direction with the dispersion relations of the isolated left and right nanoribbons superimposed as thinner lines. The thicker green lines denote the valley kink states. The plots on the right indicate the voltage amplitudes of the bands labeled i–xii in the dispersion relations at $k_y = 1.2$.

comprises 10 unit cells of the TE circuit represented by point i of Fig. 2(b) (i.e., $C_1 = 0.6$ μF, $R_v = 0.025$ μF, $C_y = 0.5$ μF) except that $C_g = 0.6$ μF on the left half and $C_g = -0.6$ μF on the right half. The facts that $|C_g| > |R_v|$ and that C_g have opposite signs on the two halves imply that the two halves of the heterojunction have finite values of the valley Hall conductivities with opposite signs. Figures 6(a) and 6(b) show that in the valley Hall regime, each half of the heterojunction in isolation has edge states (i, ii, vi, and vii) that are more substantially localized at either edge of the circuit than the bulk states (i, iv, v, and viii). When the two halves of the heterojunction are connected together [Fig. 6(c)], the edge states in the two halves localized at the edges away from the interfaces are relatively unaffected (states x and xi correspond to states ii and vi, respectively). In contrast, the edge states in the isolated segments that were originally localized near the interface (iii and vii) now hybridize to form valley kink states that are localized around the interface (ix and xii) with admittances that are substantially shifted from those of the constituent states. These valley kink states are the valley kink analogs of their Chern kink states labeled as ix and xii in Fig. 5. For this particular set of parameter values, the x and

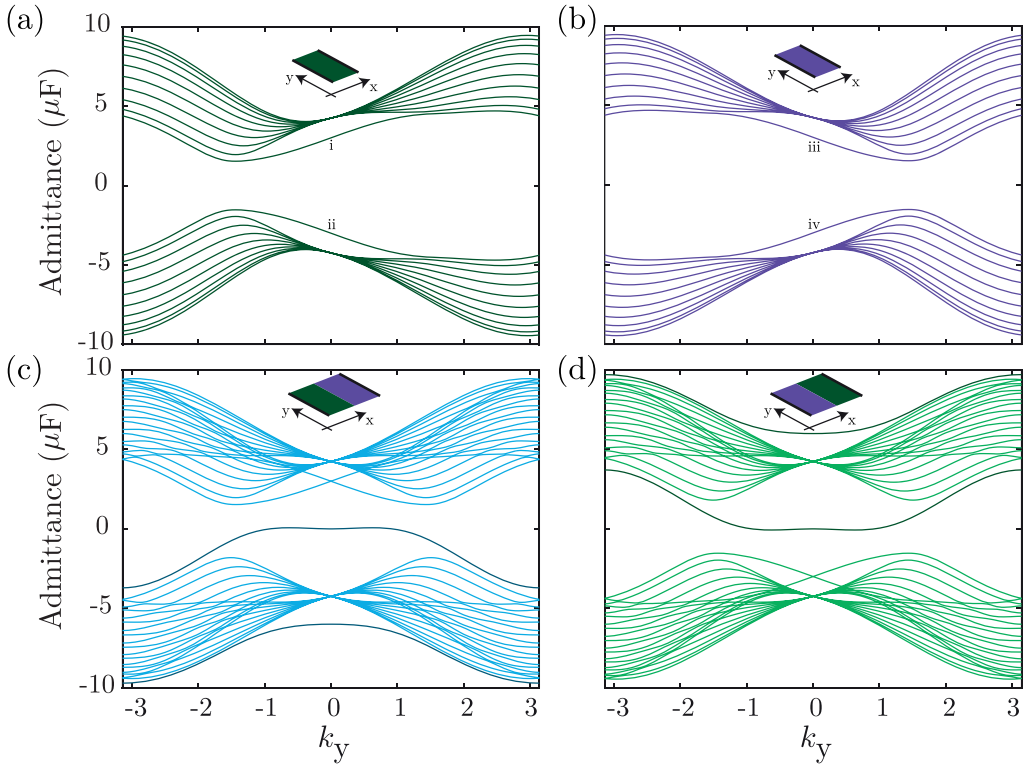

FIG. 7. Parts (a) and (b) show the band dispersions of 10-unit-cell-wide TE nanoribbons with $C_1 = 3$ μF, $R_v = 0.75$ μF, $C_y = 1.5$ μF and (a) $C_g = 3$ μF and (b) $C_g = -3$ μF. Part (c) shows the dispersion relation of the heterojunction formed when the $C_g = 3$ μF nanoribbon is on the left and the $C_g = -3$ μF nanoribbon on the right, and (d) that of the heterojunction when the $C_g = -3$ μF nanoribbon is on the left and the $C_g = 3$ μF nanoribbon on the right. The valley kink states are indicated as the darker lines in panels (c) and (d).

xi edge states that are localized away from the interface form a pair of edge states that cross the bulk band gap. It should be noted that this crossing of the bulk band gap does not necessarily occur for every parameter set inside the valley Hall regime, as we shall show in the next example.

Figure 7 shows the effect of swapping the left and right halves of the heterojunction in the valley Hall regime with another parameter set. Panels (a) and (b) show the dispersion relations for the isolated nanoribbons with positive and negative values of C_g, respectively, where $|C_g| > |R_v|$. The particlelike (holelike) edge states with positive (negative) k_y slopes, i.e., i and iv (ii and iii), are localized at the left (right) edges of the isolated nanoribbons. The dispersion relations and the energies of the kink states in the heterojunction depend on the signs of C_g in the two halves of the heterojunction. When the positive (negative) C_g nanoribbon is on the left (right) half of the heterojunction, the particlelike edge bands of both the left and right isolated halves [i.e., bands (i) and (iii)], which are localized away from the heterojunction interface, are still preserved in the heterojunction circuit, while the resultant valley kink states are holelike [i.e., bands (ii) and (iv)], as shown in Fig. 7(c). Conversely, when the negative (positive) C_g nanoribbon is on the left (right) half of the heterojunction, the holelike edge states of the isolated halves are preserved in the heterojunction circuit while the resultant valley kink states would be particlelike. Although the edge states localized away from the interface in the heterojunction do not cross the bulk gap in this instance, these edge states are still topological in nature because they arise from the valley Hall conductance, which is a topological invariant. Finally, the heterojunction circuit with the presence of Chern and valley kink states can be characterized by their unique impedance signatures, as shown in Fig. 8. Unlike the isolated nanoribbons, which exhibit only a single impedance peak as a function of k_y across the Brillouin zone, the impedance dispersion of the heterojunction circuit has a k_y-reflection symmetry that leads to a pair of impedance peaks. The impedance peaks in the impedance dispersion of the gapped valley kink heterojunction circuit are located near the points where the hole- and particlelike bands have their minimum energy separation [Fig. 8(b)], similar to the dispersion of isolated nanoribbon in Fig. 3(c). In contrast, the impedance peaks of the gapless Chern heterojunction circuit [Fig. 8(a)] are displaced from $k_y = 0$ where the hole- and particlelike bands meet. The gapless valley kink circuit [Fig. 8(c)] has a similar displacement of the main impedance peaks away from $k_y = 0$, and the main impedance peaks are substantially broader than those of the Chern heterojunction circuit. Furthermore, the peak impedance of the Chern heterojunction is much higher than its valley Hall counterparts.

V. SUMMARY

In summary, we proposed a highly tunable TE platform that exhibits topological valley Hall states, valley kink, and Chern insulating modes. The circuit can be switched between different topological Chern and valley Hall states simply by varying the sign of the on-site capacitance. Moreover, gapped

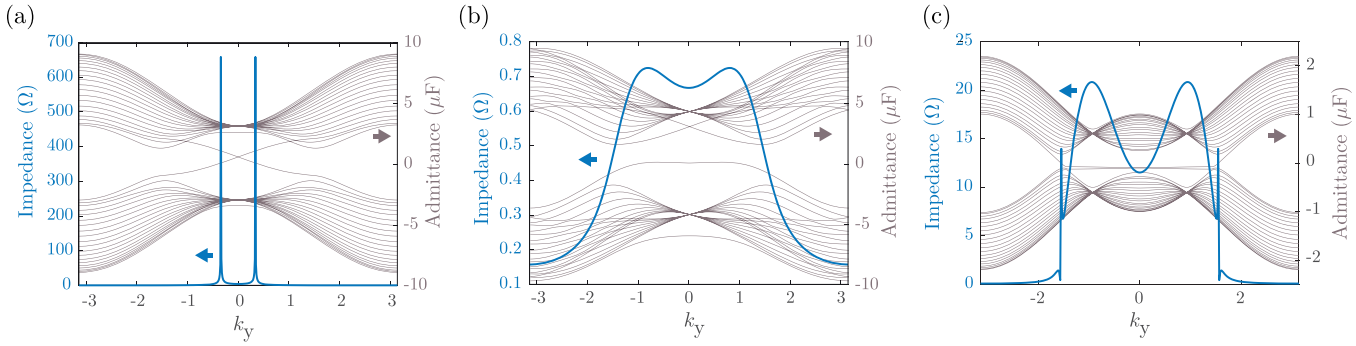

FIG. 8. Parts (a)–(c) show the band dispersions (thin lines) and the terminal impedance between the leftmost and rightmost nodes of the gapless Chern kink heterojunction in Fig. 5(c), the gapped valley kink heterojunction in Fig. 7(c), and the gapless valley kink heterojunction in Fig. 6(c), respectively.

and gapless boundary states emerge in the admittance spectra with proper tuning of the mass parameters. We also realize valley kink states by connecting two TE circuits with opposite signs of Hall conductivities together. We analytically derived the boundary conditions between the Chern and valley Hall regimes. The gapped and gapless states can be switched from one to the other by tuning the grounding capacitance. The topological boundary modes or valley kink states are localized in the interface of the kink circuit. There are significant differences in the impedance dispersion for the different boundary modes, leading to measurable and distinguishable circuit responses for different topological valley and kink states in the uniform and heterojunction TE circuits, respectively. In summary, our work based on the TE circuit model provides an accessible testbed to realize various topological valley and kink phases, and allows the efficient modulation and switching between different topological states for valleytronic applications.

ACKNOWLEDGMENTS

This work is supported by the Ministry of Education (MOE) of Singapore Tier-II Grant MOE-T2EP50121-0014 (NUS Grant No. A-8000086-01-00), and MOE Tier-I FRC Grant (NUS Grant No. A-8000195-01-00).

[1] R. Roy, Topological phases and the quantum spin Hall effect in three dimensions, Phys. Rev. B **79**, 195322 (2009).
[2] K. K. Gomes, W. Mar, W. Ko, F. Guinea, and H. C. Manoharan, Designer dirac fermions and topological phases in molecular graphene, Nature (London) **483**, 306 (2012).
[3] E. Prada, P. San-Jose, L. Brey, and H. A. Fertig, Band topology and the quantum spin Hall effect in bilayer graphene, Solid State Commun. **151**, 1075 (2011).
[4] R. Suzuki, M. Sakano, Y. Zhang, R. Akashi, D. Morikawa, A. Harasawa, K. Yaji, K. Kuroda, K. Miyamoto, T. Okuda *et al.*, Valley-dependent spin polarization in bulk mos 2 with broken inversion symmetry, Nat. Nanotechnol. **9**, 611 (2014).
[5] W. Yao, D. Xiao, and Q. Niu, Valley-dependent optoelectronics from inversion symmetry breaking, Phys. Rev. B **77**, 235406 (2008).
[6] S. M. Rafi-Ul-Islam, Z. B. Siu, H. Sahin, and M. Jalil, Valley and spin quantum Hall conductance of silicene coupled to a ferroelectric layer, Front. Phys. **10**, 1202 (2022).
[7] S. Wu, J. S. Ross, G.-B. Liu, G. Aivazian, A. Jones, Z. Fei, W. Zhu, D. Xiao, W. Yao, D. Cobden *et al.*, Electrical tuning of valley magnetic moment through symmetry control in bilayer MoS_2, Nat. Phys. **9**, 149 (2013).
[8] K. F. Mak, K. L. McGill, J. Park, and P. L. McEuen, The valley Hall effect in MoS_2 transistors, Science **344**, 1489 (2014).
[9] K. Ziegler, Robust Transport Properties in Graphene, Phys. Rev. Lett. **97**, 266802 (2006).
[10] X.-D. Chen, F.-L. Zhao, M. Chen, and J.-W. Dong, Valley-contrasting physics in all-dielectric photonic crystals: Orbital angular momentum and topological propagation, Phys. Rev. B **96**, 020202(R) (2017).
[11] J. Qi, X. Li, Q. Niu, J. Feng *et al.*, Giant and tunable valley degeneracy splitting in mote 2, Phys. Rev. B **92**, 121403(R) (2015).
[12] R. Ferdous, E. Kawakami, P. Scarlino, M. P. Nowak, D. Ward, D. Savage, M. Lagally, S. Coppersmith, M. Friesen, M. A. Eriksson *et al.*, Valley dependent anisotropic spin splitting in silicon quantum dots, npj Quantum Inf. **4**, 26 (2018).
[13] J. R. Schaibley, H. Yu, G. Clark, P. Rivera, J. S. Ross, K. L. Seyler, W. Yao, and X. Xu, Valleytronics in 2d materials, Nat. Rev. Mater. **1**, 16055 (2016).
[14] S. A. Vitale, D. Nezich, J. O. Varghese, P. Kim, N. Gedik, P. Jarillo-Herrero, D. Xiao, and M. Rothschild, Valleytronics: opportunities, challenges, and paths forward, Small **14**, 1801483 (2018).
[15] Y. Liu, Y. Gao, S. Zhang, J. He, J. Yu, and Z. Liu, Valleytronics in transition metal dichalcogenides materials, Nano Res. **12**, 2695 (2019).
[16] T. Ma and G. Shvets, All-Si valley-Hall photonic topological insulator, New J. Phys. **18**, 025012 (2016).
[17] Y. Gong, S. Wong, A. J. Bennett, D. L. Huffaker, and S. S. Oh, Topological insulator laser using valley-Hall photonic crystals, ACS Photon. **7**, 2089 (2020).

[18] B. Orazbayev and R. Fleury, Quantitative robustness analysis of topological edge modes in C6 and valley-Hall metamaterial waveguides, Nanophotonics **8**, 1433 (2019).

[19] S. Li and J. Yang, Topological Transition in Spiral Elastic Valley Metamaterials, Phys. Rev. Appl. **15**, 014058 (2021).

[20] H. Hu, W.-Y. Tong, Y.-H. Shen, X. Wan, and C.-G. Duan, Concepts of the half-valley-metal and quantum anomalous valley Hall effect, npj Comput. Mater. **6**, 1 (2020).

[21] Y. Yang, Z. Yang, and B. Zhang, Acoustic valley edge states in a graphene-like resonator system, J. Appl. Phys. **123**, 091713 (2018).

[22] W. Zhou, Y. Su, W. Chen, C. Lim *et al.*, Voltage-controlled quantum valley Hall effect in dielectric membrane-type acoustic metamaterials, Int. J. Mech. Sci. **172**, 105368 (2020).

[23] N. Rohling and G. Burkard, Universal quantum computing with spin and valley states, New J. Phys. **14**, 083008 (2012).

[24] J. Lu, C. Qiu, W. Deng, X. Huang, F. Li, F. Zhang, S. Chen, and Z. Liu, Valley Topological Phases in Bilayer Sonic Crystals, Phys. Rev. Lett. **120**, 116802 (2018).

[25] D. Culcer, A. L. Saraiva, B. Koiller, X. Hu, and S. Das Sarma, Valley-Based Noise-Resistant Quantum Computation Using Si Quantum Dots, Phys. Rev. Lett. **108**, 126804 (2012).

[26] N. Rohling, M. Russ, and G. Burkard, Hybrid Spin and Valley Quantum Computing with Singlet-Triplet Qubits, Phys. Rev. Lett. **113**, 176801 (2014).

[27] R. K. Pal and M. Ruzzene, Edge waves in plates with resonators: an elastic analogue of the quantum valley Hall effect, New J. Phys. **19**, 025001 (2017).

[28] H. Pan, Z. Li, C.-C. Liu, G. Zhu, Z. Qiao, and Y. Yao, Valley-Polarized Quantum Anomalous Hall Effect in Silicene, Phys. Rev. Lett. **112**, 106802 (2014).

[29] Q. Chen, L. Zhang, M. He, Z. Wang, X. Lin, F. Gao, Y. Yang, B. Zhang, and H. Chen, Valley-Hall photonic topological insulators with dual-band kink states, Adv. Opt. Mater. **7**, 1900036 (2019).

[30] F. Gao, H. Xue, Z. Yang, K. Lai, Y. Yu, X. Lin, Y. Chong, G. Shvets, and B. Zhang, Topologically protected refraction of robust kink states in valley photonic crystals, Nat. Phys. **14**, 140 (2018).

[31] J. Jung, F. Zhang, Z. Qiao, and A. H. MacDonald, Valley-Hall kink and edge states in multilayer graphene, Phys. Rev. B **84**, 075418 (2011).

[32] X. Ni, D. Purtseladze, D. A. Smirnova, A. Slobozhanyuk, A. Alù, and A. B. Khanikaev, Spin-and valley-polarized one-way Klein tunneling in photonic topological insulators, Sci. Adv. **4**, eaap8802 (2018).

[33] X. Zhou, Valley-dependent electron retroreflection and anomalous Klein tunneling in an 8-*pmmn* borophene-based *n-p-n* junction, Phys. Rev. B **100**, 195139 (2019).

[34] S. M. Rafi-Ul-Islam, Z. B. Siu, C. Sun, and M. B. A. Jalil, Strain-Controlled Current Switching in Weyl Semimetals, Phys. Rev. Appl. **14**, 034007 (2020).

[35] N. Stander, B. Huard, and D. Goldhaber-Gordon, Evidence for Klein Tunneling in Graphene *p-n* Junctions, Phys. Rev. Lett. **102**, 026807 (2009).

[36] S. M. Rafi-Ul-Islam, Z. B. Siu, and M. B. A. Jalil, Topoelectrical circuit realization of a Weyl semimetal heterojunction, Commun. Phys. **3**, 72 (2020).

[37] S. M. Rafi-Ul-Islam, Z. B. Siu, and M. B. Jalil, Anti-Klein tunneling in topoelectrical weyl semimetal circuits, Appl. Phys. Lett. **116**, 111904 (2020).

[38] Y. Wang, L. Deng, Q. Wei, Y. Wan, Z. Liu, X. Lu, Y. Li, L. Bi, L. Zhang, H. Lu *et al.*, Spin-valley locking effect in defect states of monolayer MoS_2, Nano Lett. **20**, 2129 (2020).

[39] Y. Saito, Y. Nakamura, M. S. Bahramy, Y. Kohama, J. Ye, Y. Kasahara, Y. Nakagawa, M. Onga, M. Tokunaga, T. Nojima *et al.*, Superconductivity protected by spin–valley locking in ion-gated MoS_2, Nat. Phys. **12**, 144 (2016).

[40] M.-J. Yang, H.-Y. Peng, N. Na, and Y.-S. Wu, Quantum state transfer between valley and photon qubits, Phys. Rev. B **95**, 075407 (2017).

[41] A. I. Lvovsky, B. C. Sanders, and W. Tittel, Optical quantum memory, Nat. Photon. **3**, 706 (2009).

[42] D. Obana, F. Liu, and K. Wakabayashi, Topological edge states in the Su-Schrieffer-Heeger model, Phys. Rev. B **100**, 075437 (2019).

[43] M. Hafezi, S. Mittal, J. Fan, A. Migdall, and J. Taylor, Imaging topological edge states in silicon photonics, Nat. Photon. **7**, 1001 (2013).

[44] S. M. Rafi-Ul-Islam, Z. B. Siu, H. Sahin, C. H. Lee, and M. B. A. Jalil, Critical hybridization of skin modes in coupled non-Hermitian chains, Phys. Rev. Res. **4**, 013243 (2022).

[45] Z. Gong, Y. Ashida, K. Kawabata, K. Takasan, S. Higashikawa, and M. Ueda, Topological Phases of Non-Hermitian Systems, Phys. Rev. X **8**, 031079 (2018).

[46] S. M. Rafi-Ul-Islam, Z. B. Siu, H. Sahin, C. H. Lee, and M. B. A. Jalil, Unconventional skin modes in generalized topolectrical circuits with multiple asymmetric couplings, Phys. Rev. Res. **4**, 043108 (2022).

[47] K. Esaki, M. Sato, K. Hasebe, and M. Kohmoto, Edge states and topological phases in non-Hermitian systems, Phys. Rev. B **84**, 205128 (2011).

[48] M. Aidelsburger, M. Lohse, C. Schweizer, M. Atala, J. T. Barreiro, S. Nascimbène, N. Cooper, I. Bloch, and N. Goldman, Measuring the Chern number of Hofstadter bands with ultracold bosonic atoms, Nat. Phys. **11**, 162 (2015).

[49] Y. Zheng and T. Ando, Hall conductivity of a two-dimensional graphite system, Phys. Rev. B **65**, 245420 (2002).

[50] L. Lu, J. D. Joannopoulos, and M. Soljačić, Topological photonics, Nat. Photon. **8**, 821 (2014).

[51] J.-W. Dong, X.-D. Chen, H. Zhu, Y. Wang, and X. Zhang, Valley photonic crystals for control of spin and topology, Nat. Mater. **16**, 298 (2017).

[52] N. Goldman, J. C. Budich, and P. Zoller, Topological quantum matter with ultracold gases in optical lattices, Nat. Phys. **12**, 639 (2016).

[53] Y. Dong, Y. Wang, C. Ding, S. Zhai, and X. Zhao, Tunable topological valley transport in acoustic topological metamaterials, J. Phys. B **605**, 412733 (2021).

[54] B. A. Bernevig, T. L. Hughes, and S.-C. Zhang, Quantum spin Hall effect and topological phase transition in HgTe quantum wells, Science **314**, 1757 (2006).

[55] S. M. Rafi-Ul-Islam, Z. B. Siu, C. Sun, and M. B. Jalil, Realization of Weyl semimetal phases in topoelectrical circuits, New J. Phys. **22**, 023025 (2020).

[56] C. H. Lee, S. Imhof, C. Berger, F. Bayer, J. Brehm, L. W. Molenkamp, T. Kiessling, and R. Thomale, Topolectrical circuits, Commun. Phys. **1**, 39 (2018).

[57] S. M. Rafi-Ul-Islam, Z. B. Siu, and M. B. A. Jalil, Topological phases with higher winding numbers in nonreciprocal one-dimensional topolectrical circuits, Phys. Rev. B **103**, 035420 (2021).

[58] T. Hofmann, T. Helbig, F. Schindler, N. Salgo, M. Brzezińska, M. Greiter, T. Kiessling, D. Wolf, A. Vollhardt, A. Kabaši *et al.*, Reciprocal skin effect and its realization in a topolectrical circuit, Phys. Rev. Res. **2**, 023265 (2020).

[59] W. Zhang, D. Zou, J. Bao, W. He, Q. Pei, H. Sun, and X. Zhang, Topolectrical-circuit realization of a four-dimensional hexadecapole insulator, Phys. Rev. B **102**, 100102(R) (2020).

[60] N. A. Olekhno, E. I. Kretov, A. A. Stepanenko, P. A. Ivanova, V. V. Yaroshenko, E. M. Puhtina, D. S. Filonov, B. Cappello, L. Matekovits, and M. A. Gorlach, Topological edge states of interacting photon pairs emulated in a topolectrical circuit, Nat. Commun. **11**, 1436 (2020).

[61] S. M. Rafi-Ul-Islam, Z. B. Siu, H. Sahin, C. H. Lee, and M. B. A. Jalil, System size dependent topological zero modes in coupled topolectrical chains, Phys. Rev. B **106**, 075158 (2022).

[62] S. Imhof, C. Berger, F. Bayer, J. Brehm, L. W. Molenkamp, T. Kiessling, F. Schindler, C. H. Lee, M. Greiter, T. Neupert *et al.*, Topolectrical-circuit realization of topological corner modes, Nat. Phys. **14**, 925 (2018).

[63] S. M. Rafi-Ul-Islam, Z. B. Siu, H. Sahin, and M. B. A. Jalil, Type-II corner modes in topolectrical circuits, Phys. Rev. B **106**, 245128 (2022).

[64] W. Zhu, Y. Long, H. Chen, and J. Ren, Quantum valley Hall effects and spin-valley locking in topological Kane-Mele circuit networks, Phys. Rev. B **99**, 115410 (2019).

[65] C. Sun, S. M. Rafi-Ul-Islam, H. Yang, and M. B. A. Jalil, Spin Nernst and anomalous Nernst effects and their signature outputs in ferromagnet/nonmagnet heterostructures, Phys. Rev. B **102**, 214419 (2020).

[66] X. Tan, Y. Zhao, Q. Liu, G. Xue, H. Yu, Z. Wang, and Y. Yu, Emulating Topological Chiral Magnetic Effects in Artificial Weyl Semimetals, Phys. Rev. Lett. **122**, 010501 (2019).

[67] S.-Z. Lin, C. D. Batista, C. Reichhardt, and A. Saxena, AC Current Generation in Chiral Magnetic Insulators and Skyrmion Motion Induced by the Spin Seebeck Effect, Phys. Rev. Lett. **112**, 187203 (2014).

[68] B.-Y. Xie, H.-F. Wang, H.-X. Wang, X.-Y. Zhu, J.-H. Jiang, M.-H. Lu, and Y.-F. Chen, Second-order photonic topological insulator with corner states, Phys. Rev. B **98**, 205147 (2018).

[69] K. Luo, R. Yu, and H. Weng, Topological nodal states in circuit lattice, Research **2018**, 6793752 (2018).

[70] S. M. Rafi-Ul-Islam, Z. B. Siu, and M. B. Jalil, Non-Hermitian topological phases and exceptional lines in topolectrical circuits, New J. Phys. **23**, 033014 (2021).

[71] K. Luo, J. Feng, Y. Zhao, and R. Yu, Nodal manifolds bounded by exceptional points on non-Hermitian honeycomb lattices and electrical-circuit realizations, arXiv:1810.09231 (2018).

[72] L. Li, C. H. Lee, and J. Gong, Emergence and full 3D-imaging of nodal boundary Seifert surfaces in 4D topological matter, Commun. Phys. **2**, 135 (2019).

[73] S. M. Rafi-Ul-Islam, H. Sahin, Z. B. Siu, and M. B. A. Jalil, Interfacial skin modes at a non-Hermitian heterojunction, Phys. Rev. Res. **4**, 043021 (2022).

[74] H. Sahin, S. M. Rafi-Ul-Islam, Z. B. Siu, C. H. Lee, and M. Jalil, Interfacial corner modes in a topolectrical heterojunction, Bull. Am. Phys. Soc. **67** (2022).

[75] T. Fukui, Y. Hatsugai, and H. Suzuki, Chern numbers in discretized Brillouin zone: efficient method of computing (spin) Hall conductances, J. Phys. Soc. Jpn. **74**, 1674 (2005).

[76] M. Tahir, A. Manchon, K. Sabeeh, and U. Schwingenschlögl, Quantum spin/valley Hall effect and topological insulator phase transitions in silicene, Appl. Phys. Lett. **102**, 162412 (2013).